

Oxygen-vacancy induced magnetic phase transitions in multiferroic thin films

Cesar Menéndez,¹ Dewei Chu,¹ and Claudio Cazorla^{1,*}

¹*School of Materials Science and Engineering, UNSW Sydney, NSW 2052, Australia*

Multiferroics in which giant ferroelectric polarization and magnetism coexist are of tremendous potential for engineering disruptive applications in information storage and energy conversion. Yet the functional properties of multiferroics are thought to be affected detrimentally by the presence of point defects, which may be abundant due to the volatile nature of some constituent atoms and high temperatures involved in materials preparation. Here, we demonstrate with theoretical methods that oxygen vacancies may enhance the functionality of multiferroics by radically changing their magnetic interactions in thin films. Specifically, oxygen vacancies may restore missing magnetic super-exchange interactions in large axial ratio phases, leading to full antiferromagnetic spin ordering, and induce the stabilization of ferrimagnetic states with a significant net magnetization of $0.5 \mu_B$ per formula unit. Our theoretical study should help to clarify the origins of long-standing controversies in bismuth ferrite and improve the design of technological applications based on multiferroics.

Finding multiferroics in which ferroelectricity and magnetism coexist and influence each other is of great fundamental and applied interests [1, 2]. Salient technological features of multiferroics include the possibility of controlling the magnetization with electric fields to design efficient logic and memory devices [3, 4], and of realizing large piezomagnetic coefficients to facilitate the miniaturization of antennas and sensors [5, 6]. Furthermore, competition between phases displaying distinct electric polarization and magnetic ordering offers also encouraging prospects for energy conversion applications like photovoltaics and solid-state cooling [7–9].

Unfortunately, multiferroics are rare in nature, typically present weak magnetoelectric coupling (BiFeO_3) [10], and require extreme synthesis conditions (PbVO_3 and BiCoO_3) [11, 12]. In addition, magnetoelectric multiferroics mostly are antiferromagnetic hence potential applications based on external magnetic bias are frustrated due to the little effect on antiparallel magnetic spins [13]. Common strategies employed to synthesize bettered multiferroic materials include doping [14, 15], solid solutions [16, 17], and strain engineering in thin films [1, 18].

Through epitaxial strain is actually possible to create new multiferroic materials in the laboratory that ex-

hibit giant electric polarization and unexpected magnetic spin ordering [19–21]. An illustrative example is given by BiFeO_3 (BFO), in which large spontaneous polarization and ferromagnetism (FM) have been observed under moderate compressive biaxial strains at room temperature [22, 23]. The origins of the net magnetization in BFO thin films, however, are not clear yet and from a technological point of view is crucially important to understand them at the fundamental level.

Most magnetic ferroelectrics with chemical formula AMO_3 and perovskite-like structure present antiferromagnetic spin ordering along the three pseudo-Cartesian directions (AFM-G), due to the dominant role of oxygen-mediated super-exchange interactions between neighbouring transition metal atoms M [24–27]. In large axial ratio structures, the covalency of M -O bonds parallel to the electric polarization is significantly reduced and consequently magnetic exchange interactions, favouring parallel magnetic spins, dominate in that direction; the coexistence of “in-plane” antiferromagnetism and “out-of-plane” ferromagnetism leads anyway to null crystal magnetization (AFM-C, Fig.1a,b) when small spin canting effects are neglected. Therefore, intrinsic and robust FM in principle is not expected to occur in BFO or any other similar multiferroic [28–31].

A plausible explanation for the appearance of FM in AMO_3 perovskite oxide thin films is based on extrinsic causes like point defects [23, 32]. The volatile nature of bismuth and high temperatures involved in the preparation of samples, for instance, make the presence of oxygen vacancies (V_O) almost inevitable in Bi-based multiferroics [15, 17]. In fact, oxygen defects may modify significantly the structural and functional properties of perovskite thin films via changes in the M oxidation states and their coupling with the lattice strain [33, 34]. However, a number of theoretical works based on first-principles methods have agreed in that the combined action of V_O and lattice strain may not affect considerably the magnetic properties of Bi-based multiferroics [35–37].

Here, we present new theoretical evidence showing that the presence of V_O may in fact change radically the magnetic properties of multiferroic thin films via previously overlooked electro-structural mechanisms. We select BiCoO_3 (BCO) as the model multiferroic in which to perform first-principles calculations based on density functional theory (DFT) because (i) this material already exhibits a large axial ratio in the absence of any strain, and (ii) the magnetic effects that we predict can be realized on substrates that are commonly employed for growth of epitaxial oxide perovskite thin films (Fig.1c). In particular, it is found that oxygen vacancies occupying specific lattice positions can induce the stabilization

* Corresponding Author

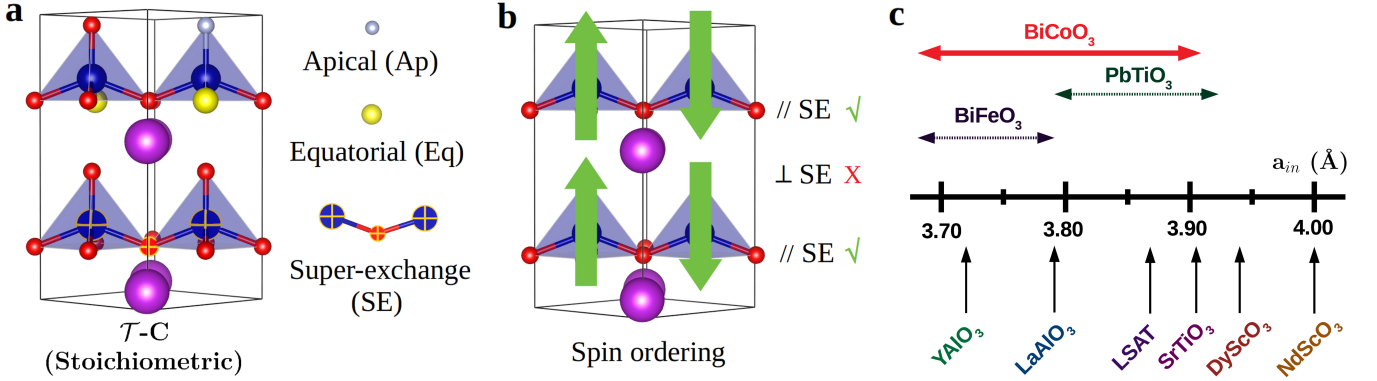


FIG. 1. Sketch of multiferroic BCO in bulk and thin film geometries. **a** Representation of the super-tetragonal phase (\mathcal{T} , space group $P4mm$) characteristic of bulk BCO and other multiferroics exhibiting giant electric polarization. **b** Magnetic structure in the \mathcal{T} phase rendering C-type antiferromagnetism (AFM-C); green arrows represent atomic magnetic moments and their orientation. **c** Examples of substrates in which to grow BCO thin films displaying the effects predicted in this study; other well-known materials exhibiting super-tetragonal phases are shown for comparison [19, 22]. “SE” stands for magnetic super-exchange interactions. Bi, Co, and O atoms are represented with magenta, blue, and red spheres, respectively.

of full antiferromagnetic (AFM-G) super-tetragonal and ferrimagnetic (FiM) monoclinic polar phases, depending on the lattice strain. As a consequence, phase competition is enriched and magnetic functionalities further enhanced in comparison to perfectly stoichiometric thin films. We show that most of the results obtained in BCO thin films can be generalized to BFO and other Bi-based multiferroics, hence our conclusions are of broad applicability and significance to the field of functional materials.

RESULTS

V_O -induced effects on phase competition and functionality. Bulk BCO presents a polar tetragonal \mathcal{T} phase with a large axial ratio of $c/a \approx 1.3$ and relatively small lattice parameter $a = 3.76$ Å [9, 29] (Fig.1a). The competing structures are a non-polar orthorhombic \mathcal{O} phase and a polar monoclinic \mathcal{M} phase (Supplementary Fig.1); both competing phases have cells that are slightly distorted versions of the ideal cubic perovskite structure with $c/a \approx 1$. The polar phases in BCO present spontaneous polarizations along quite different crystallographic directions, namely, pseudocubic $[001]_{pc}$ in \mathcal{T} and $\sim [111]_{pc}$ in \mathcal{M} . As regards magnetism, the \mathcal{O} and \mathcal{M} phases exhibit G-type antiferromagnetism (AFM-G) with a quite high Néel temperature, $T_N \approx 500$ K, whereas the \mathcal{T} phase C-type antiferromagnetism (AFM-C) with a relatively low T_N of ≈ 310 K. In stoichiometric BCO thin films, and by completely neglecting temperature effects, a multiferroic $\mathcal{T} \rightarrow \mathcal{M}$ phase transition involving large structural, polar, and magnetic changes occurs at in-plane parameter $a_{in} = 3.91$ Å [9] (Figs.2a-c).

Figures 2a-c show the influence of neutral oxygen vacancies (Methods), V_O , on the structural, ferroelectric, and magnetic properties of BCO thin films (the accompanying changes in atomic lattice positions and energy

band gap are reported in Supplementary Tables 1-4 and Supplementary Fig.2). For the smallest in-plane lattice parameters, a \mathcal{T} -C phase (magnetic spin ordering is indicated along with the structure symmetry) containing oxygen vacancies in equatorial (Eq) positions (Fig.1a) renders the lowest energy. The electric polarization and Néel temperature in \mathcal{T} -C(Eq) are significantly lower than in the analogous stoichiometric phase, in particular, we estimate differences of $\Delta P \approx -75 \mu\text{C cm}^{-2}$ and $\Delta T_N \approx -50$ K for same in-plane parameters. At $a_{in} = 3.77$ Å, an unusual magnetic phase transition from AFM-C to AFM-G spin ordering occurs along with the appearance of a small in-plane electric polarization ($P_{xy} \sim 10 \mu\text{C cm}^{-2}$) and change in V_O position symmetry. The Néel temperature in the \mathcal{T} -G(Ap) phase is lower than in \mathcal{T} -C(Eq) by approximately 50 K. Furthermore, at $a_{in} \geq 3.91$ Å the system adopts a monoclinic ferrimagnetic (FiM) phase with oxygen vacancies in equatorial positions, \mathcal{M} -FiM(Eq), and a considerable net magnetization of $\approx 0.5 \mu_B$ per formula unit (Fig.2d). The Néel temperature in the \mathcal{M} -FiM(Eq) phase is larger than in \mathcal{T} -G(Ap) and remains close to room temperature almost independently of a_{in} . (We have checked that the choice of the DFT energy functional and related technical parameters do not have a significant effect on these conclusions –Methods, Supplementary Figs.3-5, and Supplementary Methods–.)

The physical mechanisms responsible for the two multiferroic phase transitions represented in Fig.2d will be explained in detail in the next subsections. Let us now comment briefly on the functionality enhancement deriving from the \mathcal{T} -G(Ap) \rightarrow \mathcal{M} -FiM(Eq) transformation by keeping in mind that the non-stoichiometric \mathcal{M} phase is ferrimagnetic and polar hence responsive to both external magnetic and electric fields. First, a large change in the electric polarization orientation involving a $\approx 60^\circ$ rotation is observed during the transition

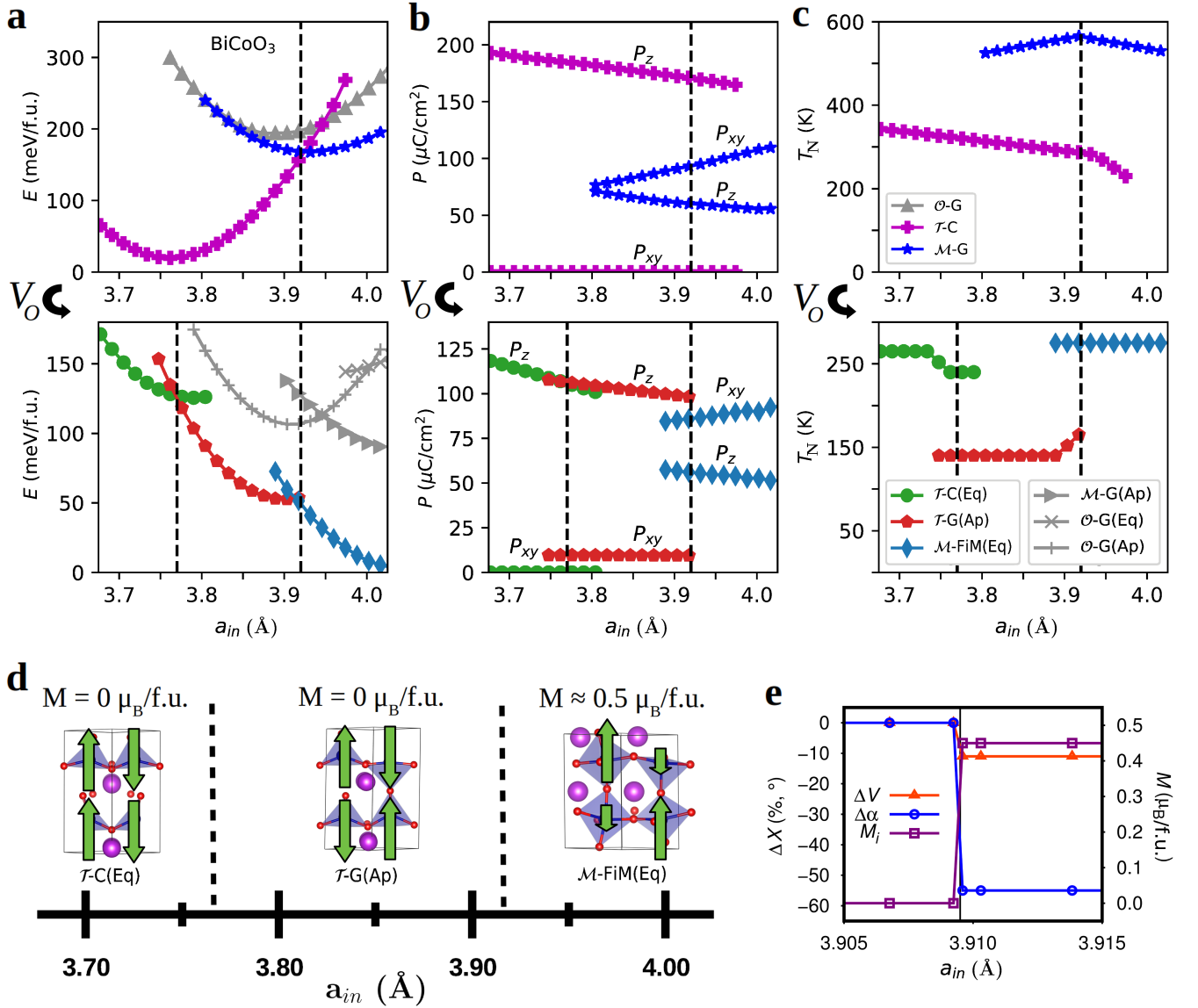


FIG. 2. Effects of V_O on phase competition and functionality in BCO thin films. **a** Zero-temperature energy of competing phases expressed as a function of in-plane lattice parameter. Metastable phases are indicated by grey curves and strain-induced phase transitions by vertical dashed lines; the oxygen vacancy positions leading to lowest energies, either apical “Ap” or equatorial “Eq”, are indicated within parentheses. “G” stands for G-type antiferromagnetism, “C” for C-type antiferromagnetism, and “FiM” for ferrimagnetism. **b** Electric polarization of stoichiometric and non-stoichiometric ground-state phases. **c** Magnetic transition temperature of stoichiometric and non-stoichiometric ground-state phases. **d** Phase transition sequence occurring in non-stoichiometric BCO thin films under increasing a_{in} ; the green arrows represent the magnetic spin ordering in each phase. **e** Change in volume, ΔV , change in electric polarization orientation, $\Delta\alpha$, and change in magnetic moment per formula unit, M_i , associated to the multiferroic $\mathcal{T}\text{-G} \rightarrow \mathcal{M}\text{-FiM}$ phase transition.

(Fig.2e); as a consequence, and in analogy to what has been observed in $\text{Pb}(\text{Zr}_{1-x}\text{Ti}_x)\text{O}_3$ alloys [38, 39] and $\text{Bi}(\text{Fe}_{1-x}\text{Co}_x)\text{O}_3$ thin films [40], it should be possible to realize large piezoelectric responses under small electric bias at $a_{in} \approx 3.91$ Å. Second, the sizeable changes in electric polarization and total magnetization in principle should allow for control of the polarization with magnetic fields and vice versa, which hints at the likely existence of large magnetoelectric couplings [1, 2]. And

third, the out-of-plane lattice parameter shrinks by an impressive $\approx 11\%$ (Fig.2e) hence there is the possibility of realizing giant piezomagnetic responses [5, 6] and multicaloric effects [8, 9] through the application of external bias. In a more speculative vein, the change in V_O position symmetry from Eq to Ap could lead to novel ionic transport phenomena driven by external magnetic, rather than electric, fields [41]. As we will show later, similar magnetic phenomena are likely to occur also in

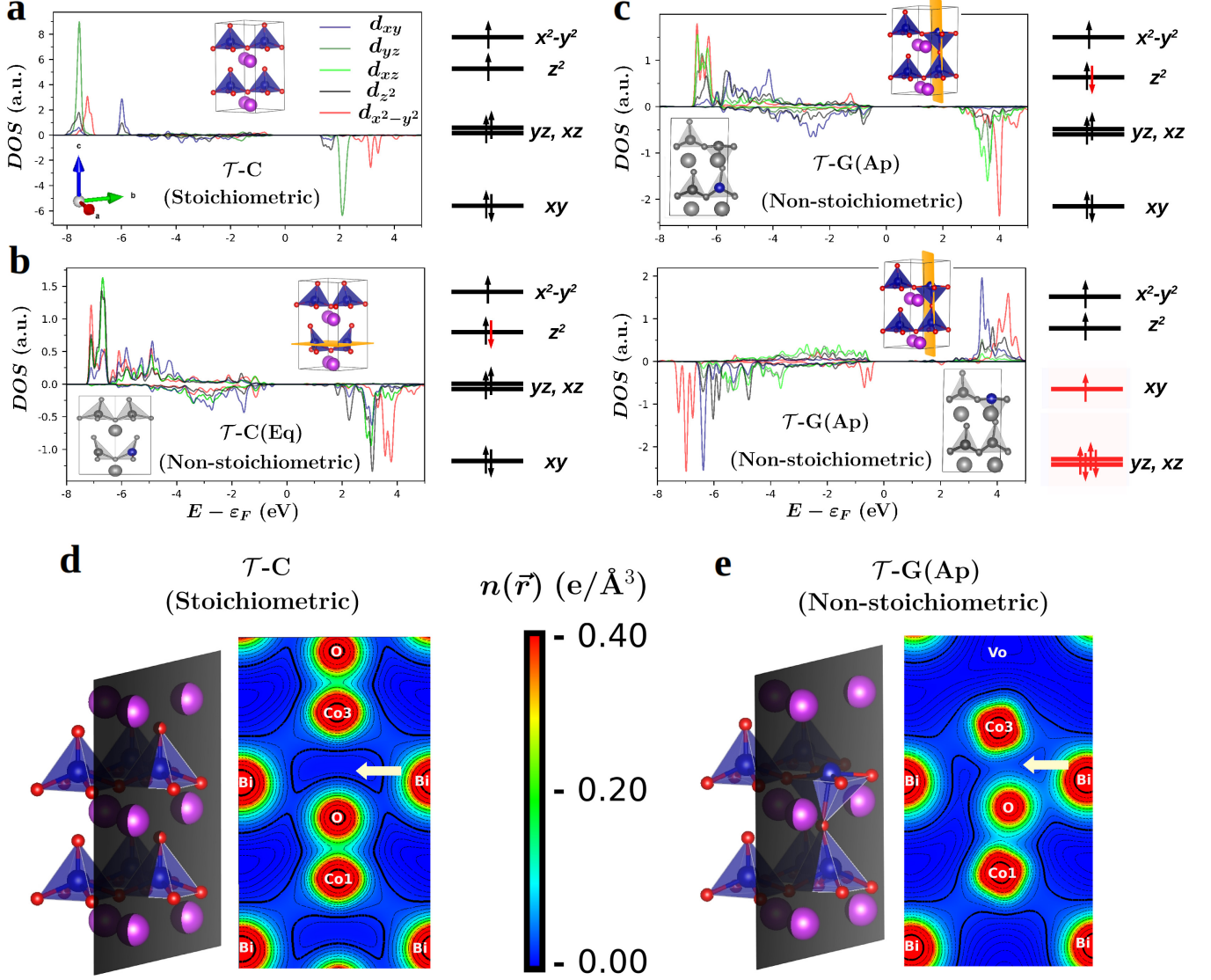


FIG. 3. Electronic, structural, and magnetic properties of \mathcal{T} BCO thin films. **a** Stoichiometric \mathcal{T} phase. **b** Non-stoichiometric \mathcal{T} thin films with a stable V_O in Eq position and AFM-C spin ordering. The orange plane indicates the two Co ions that are reduced as a consequence of creating a neutral Eq oxygen vacancy. The red arrow in the d -orbitals occupation sketch indicates the difference with respect to the stoichiometric case. **c** Non-stoichiometric \mathcal{T} thin films with a stable V_O in Ap position and AFM-G spin ordering. The orange plane indicates the two Co ions that are reduced as a consequence of creating a neutral Ap oxygen vacancy. **d** Charge density surface plot corresponding to the stoichiometric \mathcal{T} -C phase; the surface over which the charge density is calculated is indicated by a grey plane in the accompanying structural ball-stick representation. Isovalue paths are represented with black and coloured lines. **e** Charge density surface plot corresponding to the non-stoichiometric \mathcal{T} -G(Ap) phase. Regions of interest describing Co–O bonds are indicated with yellow arrows.

other Bi-based multiferroic thin films, including BiFeO₃.

V_O -induced magnetic super-exchange interactions in the \mathcal{T} phase. Figure 3 summarizes the electronic, structural, and magnetic properties of stoichiometric and non-stoichiometric \mathcal{T} BCO thin films. In the stoichiometric \mathcal{T} -C phase (Fig.3a), the square-pyramidal O₅ crystal field splits the electronic Co d levels into non-degenerate b_{2g} (d_{xy}), doubly degenerate e_g (d_{xz} , d_{yz}), and nondegenerate a_{1g} (d_{z^2}) and b_{1g} ($d_{x^2-y^2}$). Our

first-principles calculations render a high-spin Co state characterised by the electronic occupation $b_{2g}^2 e_g^2 a_{1g}^1 b_{1g}^1$ and atomic spin moment $3.1 \mu_B$, in good agreement with the available experimental data [42]. In the non-stoichiometric \mathcal{T} -C(Eq) phase (Fig.3b), the splitting of electronic d levels remains invariant with respect to the stoichiometric case and the occupation in the two cobalt ions nearest to the neutral V_O , which become reduced and are electronically equivalent, changes slightly to $b_{2g}^2 e_g^2 a_{1g}^2 b_{1g}^1$ (depending on the choice of the tech-

nical DFT parameters this electronic distribution may vary somewhat –Supplementary Fig.5 and Supplementary Methods–).

Interestingly, when V_O is created in an apical position and for specific a_{in} 's the magnetic spin ordering in the \mathcal{T} phase changes to AFM-G. Figure 3c shows the electronic density of states of the two reduced cobalt ions in the \mathcal{T} -G(Ap) phase, which in this case turn out to be electronically inequivalent. In particular, the doubly degenerate e_g (d_{xz} , d_{yz}) orbitals in the cobalt ion closest to the apical V_O (Co3, as labelled in Figs.3d,e) undergo a significant energy reduction and become fully populated rendering the occupation state $e_g^4 b_{2g}^1 a_{1g}^1 b_{1g}^1$, while the other reduced metal ion (Co1, as labelled in Figs.3d,e) exhibits the more usual distribution $b_{2g}^2 e_g^2 a_{1g}^2 b_{1g}^1$. These drastic electronic rearrangements are correlated with the appearance of a strong structural distortion in the system that pushes Co3 towards the oxygen atom underneath of it (see inversion of the corresponding O_5 square-pyramid in Figs.3c,e) and tends to restore (partially) the missing magnetic super-exchange interactions along the out-of-plane direction. This super-exchange restoration mechanism, which is accompanied by an increase in covalency of the out-of-plane Co1–O–Co3 bonds and eventually leads to the stabilization of AFM-G spin ordering, is clearly imaged by plots of the electronic density in the plane containing Co1 and Co3 and oriented perpendicular to the substrate (Figs.3d,e and yellow arrows therein).

The V_O -induced AFM-C \rightarrow AFM-G phase transition disclosed in large axial ratio BCO thin films may shed some light on uncomprehended experimental observations of antiferromagnetic spin ordering in other super-tetragonal multiferroic phases. For instance, in \mathcal{T} BFO thin films several first-principles works have predicted AFM-C spin ordering [43–45] whereas most experimental studies indicate that AFM-G dominates [46, 47]. As it will be explicitly shown later, by considering the presence of oxygen vacancies in BFO thin films those theoretical and experimental results may be reconciled.

V_O -induced stabilization of a ferrimagnetic \mathcal{M} phase. Figure 4 summarizes the electronic, structural, and magnetic properties of stoichiometric and non-stoichiometric \mathcal{M} BCO thin films. In the stoichiometric \mathcal{M} -G phase (Fig.4a), the octahedral O_6 crystal field splits the electronic Co d levels into doubly degenerate e_g (d_{z^2} , $d_{x^2-y^2}$) and triply degenerate t_{2g} (d_{xy} , d_{yz} , d_{zx}); a strong Jahn-Teller distortion rendering a large Q_2 value of 0.37 Å [48] lifts further the degeneracy in the e_g and t_{2g} manifolds [49] and promotes the electronic occupation state $b_{2g}^2 e_g^2 b_{1g}^1 a_{1g}^1$ (Fig.4a). Remarkably, when specific V_O 's are created in equatorial positions (see next paragraph) the lowest-energy magnetic spin ordering changes to FiM and the net magnetization per formula unit in the \mathcal{M} -FiM(Eq) phase amounts to $\approx 0.5 \mu_B$. The two Co ions that are reduced by the neutral vacancy present same magnetic moment orientation, same electronic oc-

cupancy $e_g^4 b_{2g}^1 b_{1g}^1 a_{1g}^1$, and sit within the $[111]_{pc}$ plane (Fig.4b).

How is possible that the two reduced Co ions are located along the diagonal of the pseudo-cubic unit cell rather than within the equatorial plane (that is, closest to the neutral V_O , in which case the total magnetization would be null)? The ground-state \mathcal{M} -FiM(Eq) phase appears only when highly magnetized oxygen atoms (0.1 – $0.2 \mu_B$) occupying equatorial positions in the stoichiometric \mathcal{M} -G crystal are removed (Fig.4c). In that case, as we sketch in Fig.4d, is not possible to reduce two neighbouring Co ions sitting in the equatorial plane (Co1 and Co2) due to Pauli exclusion principle. Consequently, pairs of metal ions with same magnetic moment and orientation (Co1 and Co4 in Fig.4d) become reduced. For the couple of distant Co1 and Co4 ions to change their oxidation state and magnetic moment, however, the crystal needs to undergo sizable structural distortions involving the Bi and O atoms surrounding V_O (Supplementary Tables 3-4). In particular, the non-magnetic oxygen atom in apical position just above Co2 acts as a bridge between the equatorial oxygen vacancy and Co4, by lending one of its electrons to the metal ion, hence reducing it, and receiving one electron from V_O (Fig.4d). This concerted electronic hopping mechanism can be inferred from plots of the electronic density in the plane containing Co1, Co2, Co3, and Co4 and oriented perpendicular to the substrate (Figs.4e,f and yellow arrows therein). As can be appreciated therein, the covalency of the Co4–O bond is significantly reduced in the \mathcal{M} -FiM(Eq) phase as compared to the stoichiometric case, and a vertical tilt of the Co2–O bond that brings the apical oxygen closer to the equatorial V_O is also evidenced.

The discovery of FiM spin ordering in the non-stoichiometric \mathcal{M} phase motivated us to search for similar magnetic states, even if metastable, in the other BCO thin film geometries \mathcal{T} and \mathcal{O} . The presence of highly magnetized O atoms was acknowledged in both stoichiometric phases (Supplementary Fig.6), however upon removal of those oxygens we did not observe the appearance of any net magnetic moment (neglecting small spin canting effects). These results confirm the importance of the electro-structural mechanisms just described on facilitating the stabilization of FiM spin ordering. For instance, in the \mathcal{T} phase the highly magnetized O atoms appear in apical positions (Supplementary Fig.6) hence the non-magnetic oxygens, which occupy equatorial positions and are somewhat clamped to the substrate, cannot act as electronic bridges between distant V_O 's and Co's. Meanwhile, in the \mathcal{O} phase, which arguably is quite similar to \mathcal{M} in terms of structure and magnetism (Supplementary Fig.1) [9, 29], the lack of polar order and high dielectric permittivity makes the enabling Bi–O structural distortions (Supplementary Table 4) to be too high in energy; consequently, FiM spin ordering is frustrated. Based on these outcomes, we propose that the following three conditions are necessary for the stabilization of V_O -induced FiM spin ordering in magnetic AMO_3 ox-

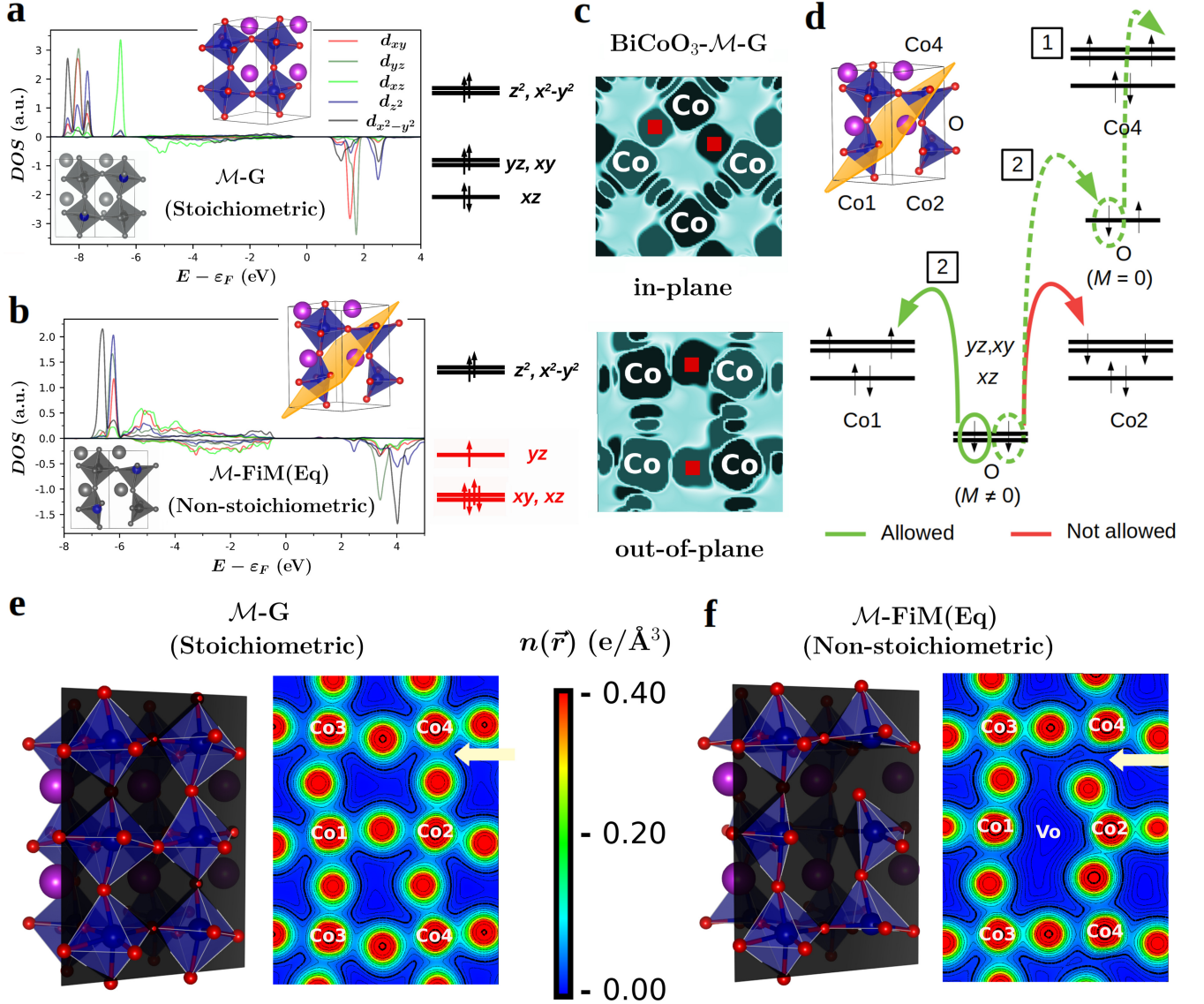


FIG. 4. Electronic, structural, and magnetic properties of \mathcal{M} BCO thin films. **a** Stoichiometric \mathcal{M} -G phase. **b** Non-stoichiometric \mathcal{M} thin films with a stable V_O in Eq position and FiM spin ordering. The orange plane indicates the two equivalent Co ions that are reduced as a consequence of creating a neutral Eq oxygen vacancy. The red arrows in the d -orbitals occupation sketch indicate the difference with respect to the stoichiometric case. **c** Spin-up (dark green) and spin-down (light green) electronic charge densities calculated in stoichiometric \mathcal{M} BCO thin films considering two perpendicular planes; highly magnetized oxygen atoms are indicated with red squares. **d** Inferred electronic hoppings enabling the stabilization of FiM spin ordering in the \mathcal{M} -FiM(Eq) phase; numbers indicate the two events that are likely to occur in a concerted manner; d orbitals a_{1g} and b_{1g} are disregarded due to their higher energies. **e** Charge density surface plot corresponding to the stoichiometric \mathcal{M} -G phase; the surface over which the charge density is calculated is indicated by a grey plane in the accompanying structural ball-stick representation. Isovalue paths are represented with black and coloured lines. **f** Charge density surface plot corresponding to the non-stoichiometric \mathcal{M} -FiM(Eq) phase. Regions of interest describing structural distortions and Co-O bonds are indicated with yellow arrows.

ide perovskites: (1) lack of inversion symmetry leading to polar order and structural deformation ease, (2) moderate axial ratio structures with $c/a \approx 1$ allowing for out-of-plane concerted electronic hoppings, and (3) the existence of highly magnetized oxygen ions.

DISCUSSION

The results obtained in BCO thin films raise the natural question: are there any other multiferroic materials in which similar V_O -induced magnetic phenomena may occur? To answer this question we investigated the spe-

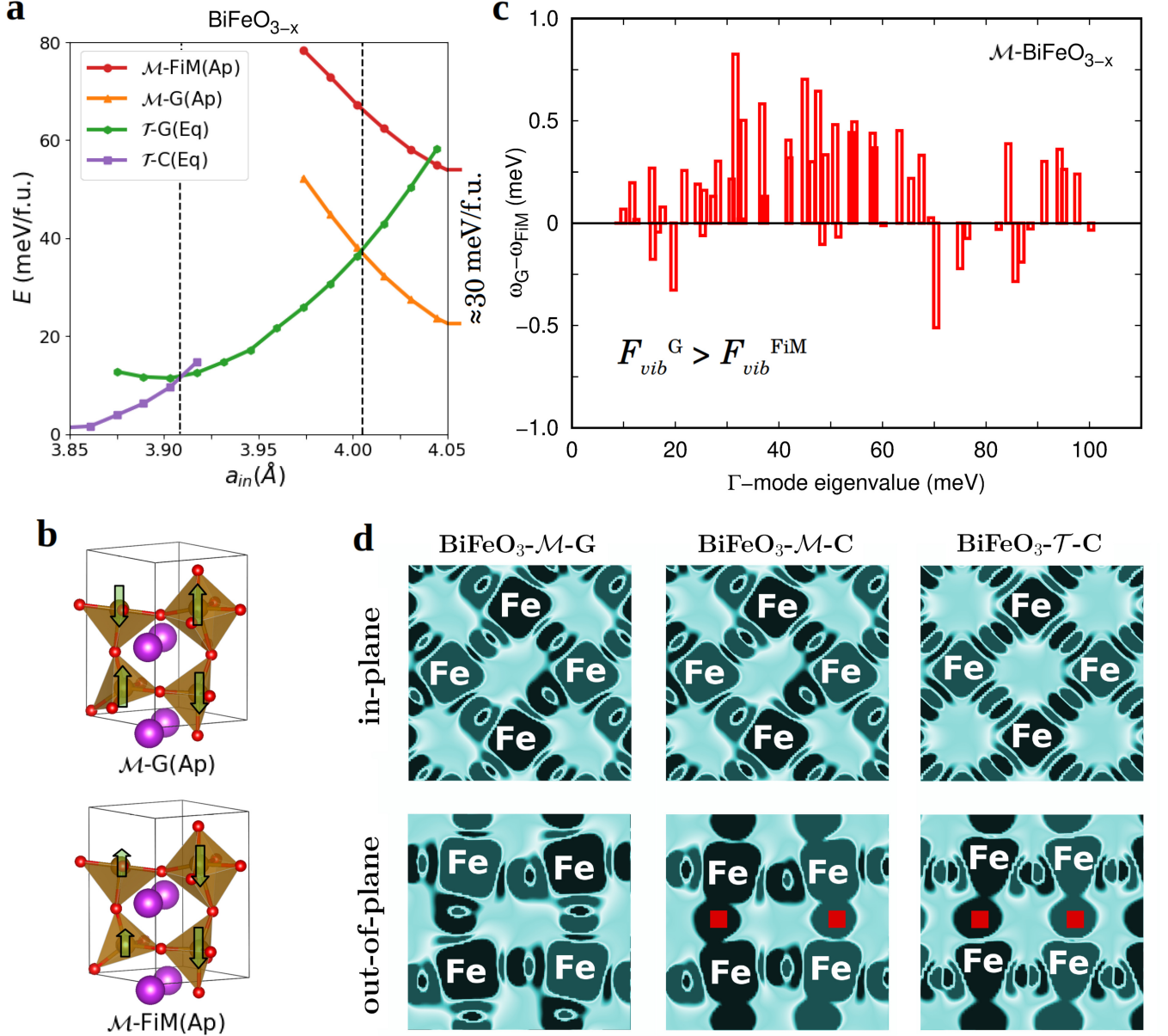


FIG. 5. Magnetic, structural, and vibrational properties of BFO thin films containing V_O . **a** Zero-temperature energy of competing phases expressed as a function of in-plane lattice parameter. **b** Structural sketch of non-stoichiometric \mathcal{M} phases considering different magnetic orderings. **c** Γ -point phonon spectrum calculated in non-stoichiometric monoclinic BFO thin films; phonon frequencies in the \mathcal{M} -G(Ap) phase are higher in average than in \mathcal{M} -FiM(Ap) hence the vibrational free energy in the latter phase is lower. **d** Spin-up (dark green) and spin-down (light green) electronic charge densities calculated in several stoichiometric BFO thin films considering two perpendicular planes; highly magnetized oxygen atoms are indicated with red squares.

cial case of BiFeO₃ (BFO) and other Bi-based multiferroic (BiMnO₃ and BiCrO₃) thin films. Figure 5 encloses the energy, magnetic, and vibrational properties of non-stoichiometric BFO thin films. In order to be consistent with the notation employed heretofore, we label the usual rhombohedral-like monoclinic phase as \mathcal{M} and the large axial ratio tetragonal-like phase as \mathcal{T} (in spite of the fact that the space groups corresponding to those structures are different in BFO and BCO) [45, 50]. Our zero-

temperature calculations (Fig.5a) predict a ground-state \mathcal{M} -G(Ap) phase at $a_{in} \geq 4.01$ Å, followed by \mathcal{T} -G(Eq) at $3.91 \leq a_{in} \leq 4.01$ Å, and \mathcal{T} -C(Eq) at $a_{in} \leq 3.91$ Å. Indeed, when the likely existence of V_O is explicitly considered in the simulations a broad a_{in} region appears in which AFM-G spin ordering is stable in the \mathcal{T} phase (that is missing in the corresponding stoichiometric system [43, 45]). The causes of the stabilization of the \mathcal{T} -G(Ap) phase in BFO are very similar to those explained

previously for \mathcal{T} -G(Ap) in BCO thin films (Fig.3; we note that Ap V_O 's under tensile strain are in some ways equivalent to Eq V_O 's under compressive strain). As mentioned earlier, these results may shed new light on the origins of some unresolved discrepancies between theory and experiments regarding the determination of antiferromagnetic ordering in \mathcal{T} BFO thin films [43–47].

By creating an apical V_O in the stoichiometric \mathcal{M} -C phase, we found a thus far neglected ferrimagnetic phase in monoclinic BFO thin films, \mathcal{M} -FiM(Ap). In this case the net magnetization per formula unit amounts also to $\approx 0.5 \mu_B$. Nevertheless, the \mathcal{M} -FiM(Ap) phase is metastable at zero temperature due to a small energy difference of 25 – 30 meV per formula unit with respect to the ground-state phase (Fig.5a). The atomic structure of the metastable \mathcal{M} -FiM(Ap) and ground-state \mathcal{M} -G(Ap) phases are highly distorted and surprisingly very similar (Fig.5b and Supplementary Tables 5-6). Analysis of the Γ -point phonon modes (Fig.5c), however, indicates that the \mathcal{M} -FiM(Ap) phase is vibrationally softer than \mathcal{M} -G(Ap). Consequently, the \mathcal{M} -FiM(Ap) phase may be entropically stabilized over \mathcal{M} -G(Ap) under increasing temperature since the zero-temperature energy difference between the two states is relatively small and the vibrational free energy of the former phase is more favourable [9, 29]. Our theoretical results, therefore, can be interpreted as evidence showing that the observation of “ferromagnetic” behaviour in BFO thin films [22] may be caused by the presence of oxygen vacancies, just as it has been suggested by other authors [23].

Figure 5d shows the spin-up spin-down charge densities calculated in non-stoichiometric \mathcal{M} and \mathcal{T} BFO thin films considering in-plane and out-of-plane surfaces. The reason why we could find just one FiM solution through the generation of neutral V_O 's in stoichiometric \mathcal{M} phases is now clear [see requirements (1)–(3) listed at the end of the previous section]: all oxygen atoms in the \mathcal{M} -G phase are non-magnetic whereas all apical O in the \mathcal{M} -C phase are highly magnetized. The stoichiometric \mathcal{T} -C phase also displays highly magnetized oxygen atoms in apical positions however, as we have explained before, FiM spin ordering hardly can be generated in geometries exhibiting $c/a \gg 1$. Furthermore, we repeated the same type of calculations and analysis in monoclinic-like BiMnO_3 and BiCrO_3 thin films, which fulfill conditions (1) and (2) explained above, and found that the appearance of FiM spin ordering is also correlated with the presence of highly magnetized oxygen atoms (Supplementary Fig.7). In particular, a \mathcal{M} -FiM(Ap) phase displaying a net magnetization of $\approx 0.2 \mu_B$ is found in BiCrO_3 . These results confirm that the simple rules provided in this work for prediction of FiM phases in non-stoichiometric multiferroic thin films are robust and general.

In summary, by using first-principles calculations we have disclosed a number of previously overlooked electrostructural mechanisms induced by the presence of oxygen

vacancies that facilitate the stabilization of unexpected magnetic states in multiferroic thin films. In particular, AFM-G and FiM spin orderings may naturally appear in large axial ratio and monoclinic phases under certain lattice strain conditions. Our theoretical results may clarify the origins of some long-standing controversies in BFO, the paradigm of single-phase multiferroics and one of the most intensively studied functional materials. We provide general and simple rules to fundamentally understand and systematically predict FiM phases in non-stoichiometric multiferroics, thus offering new approaches for the rational engineering of bettered functional materials. The present work shows that oxygen vacancies should be considered as a design opportunity to create new functionalities, especially as related to magnetism, in multiferroic thin films.

METHODS

Density functional theory calculations. First-principles spin-polarized calculations based on density functional theory (DFT) are performed with the generalized gradient approximation proposed by Perdew, Burke and Ernzerhof (GGA-PBE) as implemented in the VASP package [51, 52]. We employ the “Hubbard-U” scheme derived by Dudarev *et al.* to deal with the 3d electrons in Co (Fe) atoms and, as done in previous works, a U value of 6 (4) eV is adopted [9, 28, 29]. We use the “projected augmented wave” method [53] considering the following electronic states as valence: Co's $4s^1 3d^8$, Fe's $3p^6 4s^1 3d^7$, Mn's $4s^1 3d^6$, Cr's $4s^1 3d^5$, Bi's $6s^2 5d^{10} 6p^3$, and O's $2s^2 2p^4$. The energy cut-off is truncated at 650 eV and we employ a Γ -centered \mathbf{k} -point grid of $4 \times 6 \times 6$ for a $2 \times \sqrt{2} \times \sqrt{2}$ supercell containing 20 atoms (that is, four formula units) [50]. Periodic boundary conditions are applied along the three lattice-vector directions. Thin film geometry relaxations are carried out by using a conjugated gradient algorithm that allows to change the simulation-cell volume and atomic positions while constraining the length and orientation of the two in-plane lattice vectors. The geometry relaxations are stopped once the forces acting on the ions are smaller than 0.01 eV/Å. We have checked the vibrational stability of every phase by estimating the lattice phonons at the Γ -point with the small-displacement method [54] and considering central differences for the calculation of atomic forces derivatives.

Non-stoichiometric phases are generated by removing one oxygen atom from an apical or equatorial position in the 20-atoms simulation cell, thus rendering the chemical composition BiCoO_{3-x} with $x = 0.25$. Apical and equatorial V_O positions are investigated systematically by generating all inequivalent configurations in all competing phases and considering all possible magnetic spin orderings (FM, AFM-G, AFM-G, and AFM-A [29]). The results presented in the main text are obtained by assuming neutral oxygen vacancies since we have found

that neutral V_O 's are energetically more favourable than charged oxygen vacancies (Supplementary Fig.8, Supplementary Table 7, and Supplementary Methods). In particular, we have employed the following well-established formula to estimate the ranking of V_O formation energies as a function of charge, q , [55]:

$$E_{def}[V_O^q] = E[V_O^q] - E_{stoi} + E_{corr}^q - n_O \mu_O + q[\epsilon_F + \epsilon_v + \Delta V] , \quad (1)$$

where $E[V_O^q]$ is the energy of the non-stoichiometric system containing the oxygen vacancy, E_{stoi} the energy of the corresponding stoichiometric system, E_{corr}^q a finite-size supercell correction, n_O the number of created V_O 's (typically equal to 1 in our calculations), μ_O the chemical potential of oxygen atoms, ϵ_F the Fermi energy in the non-stoichiometric system, ϵ_v the top energy in the valence band of the non-stoichiometric system, and ΔV a term used for aligning the electrostatic potentials of the stoichiometric and defective supercells. In order to calculate E_{corr}^q and ΔV , we have followed the methods explained in work [55]. According to our estimations, neutral V_O 's ($q = 0$) are energetically more favourable than charged vacancies ($q = +2e$) by about ~ 1 eV per formula unit (Supplementary Fig.8, Supplementary Table 7, and Supplementary Methods).

We have performed several tests to assess the influence of the adopted DFT exchange-correlation functional and U value on our theoretical predictions (Supplementary Figs.3-5 and Supplementary Methods). Specifically, we repeated most calculations by considering the PBEsol functional [56] and $2 \leq U \leq 6$ eV values. It is found that the main conclusions presented in the main text are not affected qualitatively by the choice of the U parameter or exchange-correlation functional. At the quantitative level, the a_{in} parameters at which the phase transitions occur and the electronic occupations that are deduced from electronic density plots change a little in some cases (Supplementary Figs.3-5 and Supplementary Methods); however, the structural properties and energy ranking of the competing phases estimated in most a_{in} cases remain invariant. For a detailed discussion on these technical aspects, see Supplementary Methods.

Regarding the estimation of the electric polarization, P , we started by employing the Berry phase formalism [57]. However, the presence of oxygen vacancies induces a notable reduction in the energy band gap of the system (Supplementary Fig.2) that in some cases frustrates the determination of the corresponding Berry phase (due to the appearance of intermediate metallic phases). In order to overcome such a limitation, we opted for calculating the electric polarization perturbatively. Specifically, we

estimate P with the formula [50]:

$$P_\alpha = \frac{1}{\Omega} \sum_{\kappa\beta} Z_{\kappa\beta\alpha}^* u_{\kappa\beta} , \quad (2)$$

where Ω is the volume of the cell, κ runs over all the atoms, $\alpha, \beta = x, y, z$ represent Cartesian directions, \mathbf{u}_κ is the displacement vector of the κ -th atom as referred to a non-polar reference phase, and \mathbf{Z}_κ^* the Born effective charge tensor calculated in the non-polar reference state. In the stoichiometric phases we do not find the technical limitations just explained for non-stoichiometric systems, hence in that case we have been able to compare the P values obtained with the Berry phase approach (exact) and Eq.(2) (approximate). According to our estimations, the electric polarizations calculated perturbatively are accurate to within $\sim 10\%$ of, and systematically larger than, the P values calculated with the Berry phase method. It is reasonable to assume then a similar level of accuracy in the P values estimated in non-stoichiometric thin films that are reported in Fig.2.

Heisenberg model Monte Carlo simulations. To simulate the effects of thermal excitations on magnetic ordering in \mathcal{T} , \mathcal{O} , and \mathcal{M} BCO thin films, we construct several spin Heisenberg models of the form $\hat{H} = \frac{1}{2} \sum_{ij} J_{ij}^{(0)} S_i S_j$, in which the value of the involved exchange constants are obtained from zero-temperature DFT calculations (see works [9, 28, 29] for the technical details on the determination of the $J_{ij}^{(0)}$ parameters). We use those models to perform Monte Carlo (MC) simulations in a periodically-repeated simulation box of $20 \times 20 \times 20$ spins; thermal averages are computed from runs of 50,000 MC sweeps after equilibration. These simulations allow us to monitor the T -dependence of the magnetic ordering through the computation of the AFM-C (in the \mathcal{T} phase) and AFM-G (in the \mathcal{O} and \mathcal{M} phases) order parameters, namely, $S^C \equiv \frac{1}{N} \sum_i (-1)^{n_{ix}+n_{iy}} S_{iz}$ and $S^G \equiv \frac{1}{N} \sum_i (-1)^{n_{ix}+n_{iy}+n_{iz}} S_{iz}$. Here, n_{ix} , n_{iy} , and n_{iz} are the three integers locating the i -th lattice cell, and N is the total number of spins in the simulation box. For the calculation of S^C and S^G , we considered only the z component of the spins because a small symmetry-breaking magnetic anisotropy was introduced in the Hamiltonian in order to facilitate the numerical analysis [9, 28, 29].

DATA AVAILABILITY

The data that support the findings of this study are available from the corresponding author (C.C.) upon reasonable request.

[1] Ramesh, R. & Spaldin, N. A. Multiferroics: progress and prospects in thin films. *Nat. Mater.* **6**, 21 (2007).

[2] Spaldin, N. A. & Ramesh, R. Advances in magnetoelectric multiferroics. *Nat. Mater.* **18**, 203 (2019).

- [3] Heron, J. T. *et al.* Deterministic switching of ferromagnetism at room temperature using an electric field. *Nature* **516**, 370 (2014).
- [4] Allibe, J. *et al.* Room temperature electrical manipulation of giant magnetoresistance in spin valves exchange-biased with BiFeO₃. *Nano Lett.* **12**, 1141 (2012).
- [5] Domann, J. P. & Carman, G. P. Strain powered antennas. *J. Appl. Phys.* **121**, 044905 (2017).
- [6] Nan, T. *et al.* Acoustically actuated ultra-compact NEMS magnetoelectric antennas. *Nat. Commun.* **8**, 296 (2017).
- [7] Huang, W., Harnagea, C., Benetti, D., Chaker, M., Rosei, F. & Nechache, R. Multiferroic Bi₂FeCrO₆ based p-i-n heterojunction photovoltaic devices. *J. Mater. Chem. A* **5**, 10355 (2017).
- [8] Stern-Taulats, E., Castán, T., Mañosa, Ll., Planes, A., Mathur, N. D. & Moya, X. Multicaloric materials and effects. *MRS Bull.* **43**, 295 (2018).
- [9] Cazorla, C. & Íñiguez, J. Giant direct and inverse electrocaloric effects in multiferroic thin films. *Phys. Rev. B* **98**, 174105 (2018).
- [10] Bertinshaw, J. *et al.* Direct evidence for the spin cycloid in strained nanoscale bismuth ferrite thin films. *Nat. Commun.* **7**, 12664 (2016).
- [11] Belik, A. A., Azuma, M., Saito, T., Shimakawa, Y. & Takano, M. Crystallographic features and tetragonal phase stability of PbVO₃, a new member of PbTiO₃ family. *Chem. Mater.* **17**, 269 (2005).
- [12] Belik, A. A. *et al.* Neutron powder diffraction study on the crystal and magnetic structures of BiCoO₃. *Chem. Mater.* **18**, 798 (2006).
- [13] Wang, X., Yang, Q., Wang, L., Zhou, Z., Min, T., Liu, M. & Sun, N. X. Efield control of the RKKY interaction in FeCoB/Ru/FeCoB/PMNPT (011) multiferroic heterostructures. *Adv. Mater.* **30**, 1803612 (2018).
- [14] Das, R. & Mandal, K. Magnetic, ferroelectric, and magnetoelectric properties of Ba-doped BiFeO₃. *J. Magn. Magn. Mater.* **324**, 1913 (2012).
- [15] Das, R., Sharma, S. & Mandal, K. Aliovalent Ba²⁺ doping: A way to reduce oxygen vacancy in multiferroic BiFeO₃. *J. Magn. Magn. Mater.* **401**, 129 (2016).
- [16] Sakai, H. *et al.* Displacement-type ferroelectricity with off-center magnetic ions in perovskite Sr_{1-x}Ba_xMnO₃. *Phys. Rev. Lett.* **107**, 137601 (2011).
- [17] Hojo, H., Oka, K., Shimizu, K., Yamamoto, H., Kawabe, R. & Azuma, M. Development of bismuth ferrite as a piezoelectric and multiferroic material by cobalt substitution. *Adv. Mater.* **30**, 1705665 (2018).
- [18] Martin, L. W. *et al.* Multiferroics and magnetoelectrics: thinfilms and nanostructures. *J. Phys.: Condens. Matter* **20**, 434220 (2008).
- [19] Zhang, L. *et al.* Giant polarization in super-tetragonal thin films through interphase strain. *Science* **361**, 494 (2018).
- [20] Varga, T. *et al.* Coupled lattice polarization and ferromagnetism in multiferroic NiTiO₃ thin films. *ACS Appl. Mater. Interfaces* **9**, 21879 (2017).
- [21] Töpfer, J. & Goodenough, J. G. LaMnO_{3+δ} revisited. *J. Solid State Chem.* **130**, 117 (1997).
- [22] Wang, J. *et al.* Epitaxial BiFeO₃ multiferroic thin film heterostructures. *Science* **299**, 1719 (2003).
- [23] Eerenstein, W., Morrison, F. D., Dho, J., Blamire, M. G., Scott, J. F. & Mathur, N. D. Comment on “Epitaxial BiFeO₃ multiferroic thin film heterostructures”. *Science* **307**, 1203 (2005).
- [24] Goodenough, J. B. Theory of the role of covalence in the perovskite-type manganites (La,M(II))MnO₃. *Phys. Rev.* **100**, 564 (1955).
- [25] Hill, N. A. & Filipetti, A. Why are there any magnetic ferroelectrics?. *J. Magn. Magn. Mater.* **242**, 976 (2002).
- [26] Spaldin, N. A. *Magnetic Materials: Fundamentals and Applications*. Second Edition, Cambridge University Press, doi:10.1017/CBO9780511781599.021 (2012).
- [27] Bhattacharya, A. & May, S. Magnetic oxide heterostructures. *Annu. Rev. Mater. Res.* **44**, 65 (2014).
- [28] Cazorla, C. & Íñiguez, J. Insights into the phase diagram of bismuth ferrite from quasi-harmonic free-energy calculations. *Phys. Rev. B* **88**, 214430 (2013).
- [29] Cazorla, C., Diéguez, O. & Íñiguez, J. Multiple structural transitions driven by spin-phonon couplings in a perovskite oxide. *Sci. Adv.* **3**, e1700288 (2017).
- [30] Singh, D. J. Electronic structure and bond competition in the polar magnet PbVO₃. *Phys. Rev. B* **73**, 094102 (2006).
- [31] Solovyev, I. V. Magnetic structure of the noncentrosymmetric perovskites PbVO₃ and BiCoO₃: Theoretical analysis. *Phys. Rev. B* **85**, 054420 (2012).
- [32] Niu, W. *et al.* Direct demonstration of the emergent magnetism resulting from the multivalence Mn in a LaMnO₃ epitaxial thin film system. *Adv. Electron. Mater.* **4**, 1800055 (2018).
- [33] Cazorla, C. Lattice effects on the formation of oxygen vacancies in perovskite thin films. *Phys. Rev. Appl.* **7**, 044025 (2017).
- [34] Herklotz, A. *et al.* Strain coupling of oxygen non-stoichiometry in perovskite thin films. *J. Phys.: Condens. Matter* **29**, 493001 (2017).
- [35] Ederer, C. & Spaldin, N. A. Influence of strain and oxygen vacancies on the magnetoelectric properties of multiferroic bismuth ferrite. *Phys. Rev. B* **71**, 224103 (2005).
- [36] Paudel, T. R., Jaswal, S. S. & Tsymbal, E. Y. Intrinsic defects in multiferroic BiFeO₃ and their effect on magnetism. *Phys. Rev. B* **85**, 104409 (2012).
- [37] Chen, X.-Y., Chen, L.-J., Yang, X.-B., Zhao, Y.-J., Ding, H.-C. & Duan, C.-G. Tuning the polarization and magnetism in BiCoO₃ by strain an oxygen vacancy effect: A first-principle study. *J. Appl. Phys.* **111**, 013901 (2012).
- [38] Jaffe, B., Roth, R. S. & Marzullo, S. Piezoelectric properties of lead zirconate-lead titanate solid solution ceramics. *J. Appl. Phys.* **25**, 809 (1954).
- [39] Bellaiche, L., García, A. & Vanderbilt, D. Finite-temperature properties of Pb(Zr_{1-x}Ti_x)O₃ alloys from first principles. *Phys. Rev. Lett.* **84**, 5427 (2000).
- [40] Shimizu, K., Hojo, H., Ikuhara, Y. & Azuma, M. Enhanced piezoelectric response due to polarization rotation in cobalt-substituted BiFeO₃ epitaxial thin films. *Adv. Mater.* **28**, 8639 (2016).
- [41] Waskaas, M. & Kharkats, Y. I. Magnetoconvection phenomena: A mechanism for influence of magnetic fields on electrochemical processes. *J. Phys. Chem. B* **103**, 4876 (1999).
- [42] Oka, K. *et al.* Pressure-induced spin-state transition in BiCoO₃. *J. Am. Chem. Soc.* **132**, 9438 (2010).
- [43] Hatt, A. J., Spaldin, N. A. & Ederer, C. Strain-induced isosymmetric phase transition in BiFeO₃. *Phys. Rev. B* **81**, 054109 (2010).

- [44] Diéguez, O., González-Vázquez, O. E., Wojdel, J. C. & Íñiguez, J. First-principles predictions of low-energy phases of multiferroic BiFeO₃. *Phys. Rev. B* **83**, 094105 (2011).
- [45] Heo, Y. *et al.* Impact of isovalent and aliovalent doping on mechanical properties of mixed phase BiFeO₃. *ACS Nano* **11**, 2805 (2017).
- [46] Béa, H. *et al.* Evidence for room-temperature multiferroicity in a compound with a giant axial ratio. *Phys. Rev. Lett.* **102**, 217603 (2009).
- [47] MacDougall, G. J. *et al.* Antiferromagnetic transitions in tetragonal-like BiFeO₃. *Phys. Rev. B* **85**, 100406 (2012).
- [48] Rivero, P. & Cazorla, C. Revisiting the zero-temperature phase diagram of stoichiometric SrCoO₃ with first-principles methods. *Phys. Chem. Chem. Phys.* **18**, 30686 (2016).
- [49] Halcrow, M. A. Jahn-Teller distortions in transition metal compounds, and their importance in functional molecular and inorganic materials. *Chem. Soc. Rev.* **42**, 1784 (2013).
- [50] Cazorla, C. & Stengel, M. Electrostatic engineering of strained ferroelectric perovskites from first principles. *Phys. Rev. B* **92**, 214108 (2015).
- [51] Kresse, G. & Furthmüller, J. Efficient iterative schemes for ab initio total-energy calculations using a plane-wave basis set. *Phys. Rev. B* **54**, 11169 (1996).
- [52] Perdew, J. P., Burke, K. & Ernzerhof, M. Generalized gradient approximation made simple. *Phys. Rev. Lett.* **77**, 3865 (1996).
- [53] Blöchl, P. E. Projector augmented-wave method. *Phys. Rev. B* **50**, 17953 (1994).
- [54] Cazorla, C. & Boronat, J. Simulation and understanding of atomic and molecular quantum crystals *Rev. Mod. Phys.* **89**, 035003 (2017).
- [55] Komsa, H.-P., Rantala, P. P. & Pasquarello, A. Finite-size supercell correction schemes for charged defect calculations. *Phys. Rev. B* **86**, 045112 (2012).
- [56] Perdew, J. P. *et al.* Restoring the density-gradient expansion for exchange in solids and surfaces. *Phys. Rev. Lett.* **100**, 136406 (2008).
- [57] King-Smith, R. D. & Vanderbilt, D. Theory of polarization of crystalline solids. *Phys. Rev. B* **47**, 1651(R) (1993).

ACKNOWLEDGMENTS

Computational resources and technical assistance were provided by the Australian Government and the Government of Western Australia through the National Computational Infrastructure (NCI) and Magnus under the National Computational Merit Allocation Scheme and The Pawsey Supercomputing Centre.

AUTHOR CONTRIBUTIONS

C.C. conceived the study and planned the research. C.M. and C.C. performed the theoretical calculations. Results were discussed by C.M., D.C., and C.C. The manuscript was written by C.M., D.C., and C.C.

ADDITIONAL INFORMATION

Supplementary information is available in the online version of the paper.

COMPETING INTERESTS

The authors declare no competing interests.